Research Article

Dielectric relaxation and magnetodielectric response of mesoporous terbium manganate nanopaticles

Monalisa Halder[1] · Ajit Kumar Meikap[1]

Abstract

We report here the investigation on dielectric response, charge transport mechanism and magnetocapacitance of mesoporous perovskite Terbium Manganate (TMO) nanoparticles. TMO NPs possess relatively high specific surface area (20.9 $m^2 g^{-1}$) than that of general perovskite-type metal oxides. To study the dielectric/magnetodielectric response in TMO material, a capacitive system is fabricated. Impedence spectroscopy shows electrically heterogeneous nature of the material. Due to the existence of inhomogeneity at electrode-TMO interface, ideality factor is larger than unity. Various Schottky diode electrical parameters are obtained here from temperature dependent capacitance–voltage (C–V) measurements. The function of Au/TMO/Au Schottky diode system is well explained from current–voltage (I–V) characteristics study. Ferroelectric-like hysteretic behaviour is observed at and above room temperature from non-ferroelectric TMO. Presence of defect states at TMO interface layer dominates the charge conduction phenomenon. Negative magnetodielectric effect arises in heterogeneous TMO sample due to the effect of magnetic field on Maxwell–Wagner space charge at the interface.

Graphic abstract The thermionic current–voltage (I–V) characteristics of the Au/TMO/Au Schottky diode have been measured within the voltage range ± 40 V. Ferroelectric type hysteretic behaviour is observed in non-ferroelectric TMO sample.
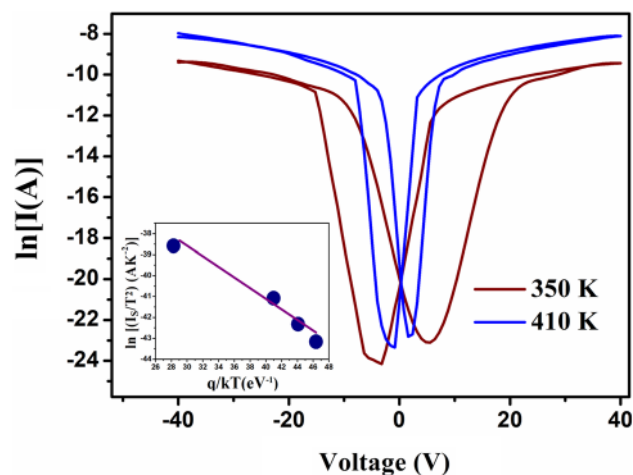
1 Introduction

Rare-earth manganites are a major class of perovskite structured multiferroic materials due to the co-existance of both ferroelectricity and magnetism [1, 2]. Due to their multifunctional properties, they have potential applications for smaller and faster electronic devices as well as high energy storage devices [3, 4]. Terbium manganate ($TbMnO_3$) is an interesting rare-earth manganite multiferroic material, that exhibits orthorhombically distorted perovskite structure at room temperature [5, 6]. Perovskite-type metal oxide compounds [general formula = ABX_3] are considered to be an important class of materials for catalytic oxidations and reductions and solar cell applications [7, 8]. But the major challenge is that perovskite-type materials generally show very small surface area ($< 2 \ m^2 \ g^{-1}$), which in turn lowers the specific catalytic activity [9]. Researchers are interested to achieve nanomaterials with higher specific surface area. Ahmad et al. reported high specific surface area ($304 \ m^2 \ g^{-1}$) of multiferroic $YMnO_3$ nanoparticles [10]. Silva et al. investigated the catalytic activity of perovskite-type oxides with different surface areas of 33–$44 \ m^2 \ g^{-1}$ [7]. They can be utilised in various applications such as non-volatile memories, solar cells, photovoltaics and light polarisers [11]. Size-morphology dependent magnetic-dielectric behaviour study of multiferroics are in trend [12]. As differed from the properties present in bulk materials, it is very much important to investigate the magnetic and electrical behaviours of the materials at nanoscale region. Discovery of ferroelectric control of magnetic order in perovskite $TbMnO_3$ invoked intensive researches in the field of magnetodielectric materials [13]. Gupta et al. [14] reported magneto-structural and magneto-electric coupling in multiferroic $BiFeO_3$–$TbMnO_3$ composite. Acharya et al. [12] reported the multiferroic behaviour of hydrothermally prepared $TbMnO_3$ nanoplates. Lu et al. [15] reported the dielectric characteristics of polycrystalline Si-added and Si-doped $TbMnO_3$ materials. Izquierdo et al. [16] reported the dielectric response of Al-subsituted multiferroic $TbMnO_3$ at high temperatures. But there are very few articles on the investigation of dielectric response and defect state contribution in the electrical transport properties of TMO NPs.

The present article reports the morphological, electrical and magnetodielectric characteristics of $TbMnO_3$ (TMO) NPs. BET (Brunauer–Emmett–Teller) analysis and BJH (Barrett–Joyner–Halenda) analysis are done to get the idea of surface morphology of the material. Here frequency dependent dielectric response of TMO NPs is studied above room temperature and the behaviours have been well explained by suitable theories. Voltage dependent capacitance (C–V) and voltage dependent current (I–V) measurements of the sample are done above room temperature. In this work, various electrical parameters are evaluated to get the information about the current conduction mechanism in the material. Further at room temperature, we have observed significant negative magnetodielectric (MD) response of the material.

2 Experimental details

Detailed synthesis procedure of mesoporous Terbium manganate (TMO) NPs and its physical characterisations are reported earlier [17]. In the present work, room temperature Fourier transform infrared spectrum (FTIR) of the sample (in pellet form milled with KBr) is recorded with FT-IR spectrometer (Thermo Nicolet iS10) in the region of 400–$4000 \ cm^{-1}$. The porosity and Brunaur–Emmett–Teller (BET) surface area of the sample is determined by N_2 physisorption measurements by Autosorb IQ gas sorption analyser (Quantachrome Instruments Cooperation). Electrical measurements of the sample are studied by making pellet of sample of area $2.83 \times 10^{-5} \ m^2$ and thikness $9.2 \times 10^{-3} \ m$. Conducting layer of silver is coated on opposite sides of the pellet to serve as electrodes. To study the electrical properties of the sample above room temperature, an oven with a temperature controller cryostat is used above room temperature. Dielectric measurements are carried out at frequencies ranging from 20 Hz–2 MHz on Agilent E 4980A LCR meter. The capacitance–voltage (C–V) is measured under 2 MHz frequency above room temperature. The I–V characteristic of the sample is obtained by applying a DC field and using computer controlled Keithley source meter (SMU). Susceptibility measurement of TMO NPs is carried out by Magnetic Susceptibility Balance (Sherwood). Using an electromagnet (EM-250), magnetodielectric measurements are done with the variation of the external transverse magnetic field ($H \leq 1 \ T$).

3 Results and discussions

Figure 1 shows FESEM micrograph of TMO NPs of non-uniformly distributed grains. Less dense microstructure is obsereved. The grains are mesoporous in nature.

FT-IR study is performed here to substantiate the formation of TMO NPs and the organic residue on the sample (Fig. 2). The absorption peaks centered at $492 \ cm^{-1}$ and $590 \ cm^{-1}$ are the characteristic peaks of Mn–O–Mn bond bending vibration and Mn–O bond stretching vibration of perovskite-type structured Terbium Manganate
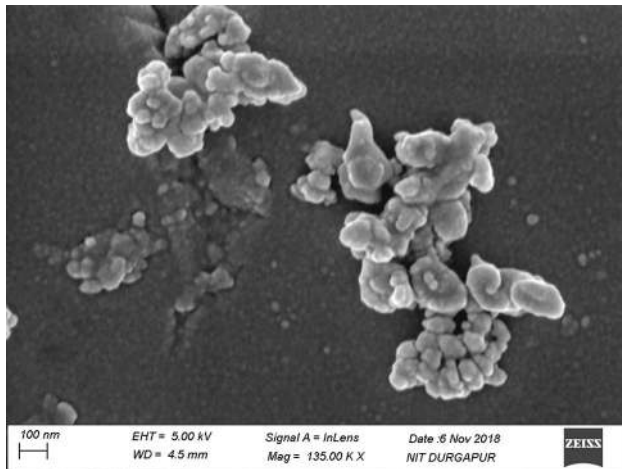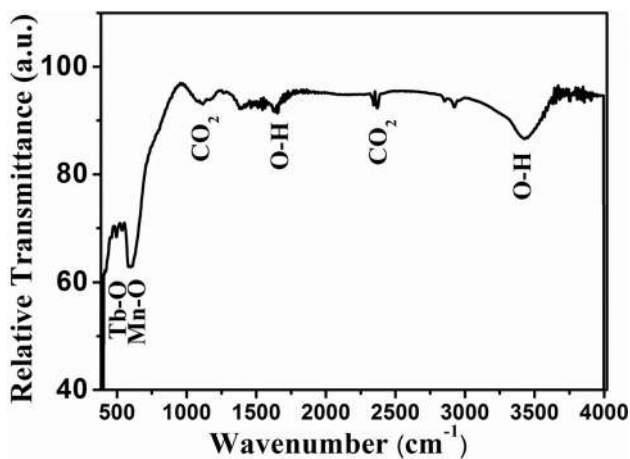
Fig. 1 FESEM image of TMO NPs

Fig. 2 Room temperature FT-IR spectrum of the sample

Fig. 3 **a** N_2 adsorption–desorption isotherms of TMO NPs at 77 K (the inset displays the enlarged view of the isotherm at high p/p_0), **b** BET plot of the sample at 77 K

respectively [18, 19]. A peak centered at 1645 cm^{-1} comes from the bending vibration of O–H bond of adsorbed water molecule in the sample [19]. A strong absorption band centered at 3430 cm^{-1} corresponds to the O–H stretch vibration of water [18]. Peaks centered at 1110 cm^{-1} and 2356 cm^{-1} come from the CO_2 content present in the atmosphere [20].

The surface morphology is observed from BET analysis and the N_2 adsorption/desorption isotherms. The total mass of the sample present during this analysis was approximately 3.78 mg. The isotherms are measured under the relative pressure region (p/p_0) from 0.1 to 1.0 and back. Isotherm is a physisorption experiment that provides the information about the surface and porosity of the material [21]. Figure 3a exhibits N_2 adsorption/desorption isotherms of TMO NPs at 77 K. The measured isotherm can be classified as Type II isotherm in Brunauer
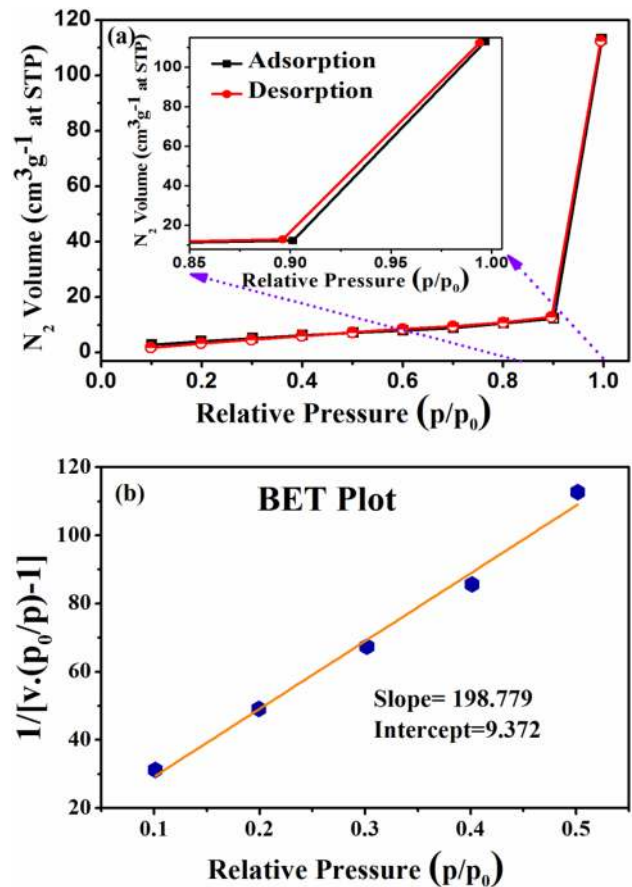
classification [22, 23]. This type isotherm generally represents unrestricted monolayer-multilayer adsorption [24]. From the graph, it can be shown that the adsorption and desorption isotherms superpose to each other indicating mostly micropore related adsorption [25]. The increase in adsorbed gas volume at high value of p/p_0 takes place due to the capillary condensation [21]. Brunauer–Emmett–Teller (BET) specific surface area (S_{BET}) and monolayer adsorption volume (V_m) are calculated using BET equation as follows [26],

$$\frac{p}{V_{ads}(p_0 - p)} = \frac{1}{V_m C_B} + \frac{C_B - 1}{V_m C_B}\left(\frac{p}{p_0}\right), \qquad (1)$$

where V_{ads} is the adsorbed N_2 volume, p and p_0 are the equilibrium and saturated vapour pressure of adsorbates at adsorption temperature respectively, C_B is a constant and V_m is the monolayer adsorbed N_2 volume. BET specific surface area (S_{BET}) is determined using the relation $S_{BET} = 4.355 \times V_m$. Considering the particle to be spherical,

average particle size $\left(D_{BET}\right)$ can be calculated using the following equation [25, 26],

$$D_{BET} = \frac{6000}{\rho \times S_{BET}}, \tag{2}$$

where $\rho = 7.36$ g/cc, the crystallographic density of TMO NPs. BET plot of the NPs is exhibited in Fig. 3b. Parameter C_B can be calculated as,

$$C_B = \frac{Slope}{Intercept} + 1. \tag{3}$$

The C_B parameter measures the strength of the interaction of the adsorbate (N_2) with the surface of the material [27].

The calculated parameters such as specific surface area $\left(S_{BET}\right)$, monolayer adsorbed N_2 volume $\left(V_m\right)$ and average particle size $\left(D_{BET}\right)$ are indexed in Table 1. In case of multilayer adsorption, on the pore walls, an adsorbed layer has formed which is responsible for capillary condensation at higher p/p_0 [26]. The adsorbed layer thickness (t) is derived from the adsorption isotherm data as follows [28],

$$t = \left(\frac{13.99}{-\log\left(p/p_0\right) + 0.034}\right)^{1/2}. \tag{4}$$

The plot of V_{ads} versus t is known as $t - plot$, which is shown in Fig. 4a. The slope of the straight portion gives the value of cumulative pore surface area $\left(S_{t-plot}\right)$ for multilayer adsorption because S_{t-plot} is related by the equation,

$$t = V_{ads}/S_{t-plot}. \tag{5}$$

Pore size distribution from both the adsorption and desorption branches of isotherm data generally is described by Barrett–Joyner–Halenda (BJH) analysis [21]. In general, the pores of the material can be categorised as micropores (size < 2 nm), mesopores (2–50 nm) and macropores (> 50 nm) [29]. To fit BJH model, the pores are considered here as cylindrical. The average pore diameter $\left(r_p\right)$ can be
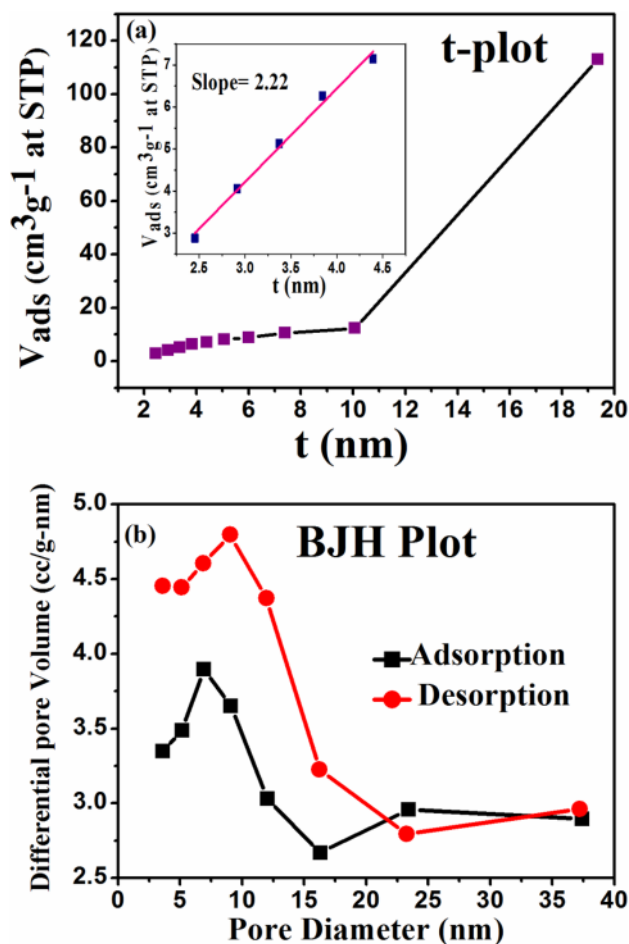

Fig. 4 **a** t- plot for TMO NPs at 77 K (the inset displays the linear portion of $t - plot$ curve), **b** differential pore size distribution curve (BJH plot) of TMO NPs for adsorption and desorption branch

calculated using Kelvin equation and $t - plot$ equation such as [21],

$$r_p = r_K + t, \tag{6}$$

Table 1 The derived surface parameters of TMO NPs derived from BET plot, $t - plot$ and pore size distribution (BJH plot) analysis

BET plot ananlysis		t-plot & pore size distribution (BJH Plot) analysis	
Parameter	Value	Parameter	Value
Constant $\left(C_B\right)$	22.21	Cumulative surface area of pore $\left(S_{t-plot}\right)$	22.23 m^2 g^{-1}
Monolayer adsorption volume $\left(V_m\right)$	4.80 cm^3 g^{-1} at STP	Cumulative pore volume $\left(V_{pore}\right)$	0.17 cm^3 g^{-1} at $p/p_0 = 0.99$
BET specific surface area $\left(S_{BET}\right)$	20.90 m^2 g^{-1}	Average pore diameter $\left(d_{pore}\right)$	7 nm (for adsorption branch) 9 nm (for desorption branch)
Average particle size $\left(D_{BET}\right)$	39 nm		

where r_K is the Kelvin radius i.e. the radius of the condensed adsorbate and t is the adsorbed layer thickness. The differential pore size distribution curve (BJH plot) of TMO NPs is shown in Fig. 4b, which clearly indicates the mesoporosity present in the sample. This is single modal distribution centred at ~ 7 nm for adsorption branch (~ 9 nm for desorption branch).The pore size distribution derived from adsorption branch is quite similar with that obtained from the adsorption branch. These unique pores can effectively provide disorder-free paths for oxygen vacancies for catalytic performances [29]. Based on $t - plot$ and BJH analysis, the values of cumulative surface area of pore $\left(S_{t-plot}\right)$, cumulative pore volume $\left(V_{BJH}\right)$ and average pore diameter $\left(d_{BJH}\right)$ are evaluated and listed in Table 1 [27]. Soleymani et al. [30] reported the synthesis of nano-sized $La_{0.6}Ca_{0.4}MnO_3$ with high specific surface area (40.7 m^2 g^{-1}) by low temperature pyrolysis of a modified citrate gel method. Rabelo et al. [31] reported the synthesis of pure phase perovskite $La_{1-x}Sr_xMnO_{3\pm\delta}$ with specific surface area of 34.3 m^2 g^{-1} which is potentially applicable for solid oxide fuel cells (SOFC). In the present work, we have achieved the specific surface area of 20.9 m^2 g^{-1} of the synthesised TMO NPs.

Further the dielectric response of this sample to an alternating applied electric field is recorded. The application of electric field produces/alters the net dipole moment density in the material. In this case, the change in the positive–negative charge orientations will not be instantaneous. The frequency dependent dielectric constant is expressed as,

$$\varepsilon^*(f) = \varepsilon'(f) - i\varepsilon''(f). \tag{7}$$

The frequency dependent real part $[\varepsilon'(f)]$ and imaginary part $[\varepsilon''(f)]$ of dielectric constant respectively (Fig. 5a, b). The $\varepsilon'(f)$ and $\varepsilon''(f)$ values are high in the lower frequency region due to the effect of electrode polarisation. In the higher frequencies, the free ions in the material cannot find sufficient time to direct themselves along the field direction. As a result th values of $\varepsilon'(f)$ and $\varepsilon''(f)$ become lower in this range. At lower temperature region, size of the micro domains increases as they fuse together. As a result delay of the response to the applied field takes place. The experimental data of dielectric relaxation process can be described by the following Cole–Cole function [32, 33],
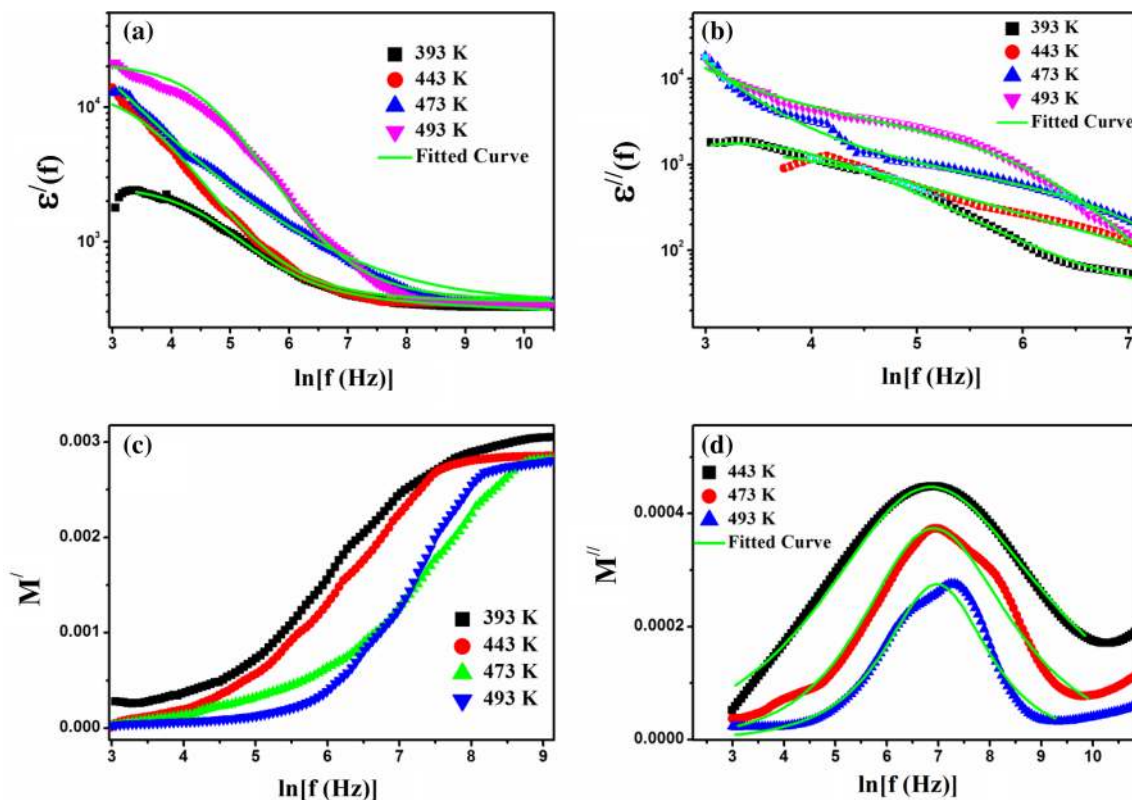
Fig. 5 **a** The frequency variation of $[\varepsilon'(f)]$ of the sample at different temperatures, **b** the frequency variation of $[\varepsilon''(f)]$ of the sample at different temperatures, **c** the frequency variation of real part (M') of complex electric modulus of the sample at different temperatures, **d** the frequency variation of imaginary part (M'') of complex electric modulus of the sample at different temperatures

$$\varepsilon^*(f) = \varepsilon_\infty + \frac{\varepsilon_S - \varepsilon_\infty}{1 + (i\omega\tau)^\beta} - \frac{i\sigma^*}{\varepsilon_0 \omega^p}, \tag{8}$$

where β and p describe the 'skewdness' and the 'depression' of relaxation time distribution respectively. ε_S and ε_∞ are the static and infinite dielectric constant respectively, the dielectric relaxation time is τ. The expression of $\varepsilon'(f)$ and $\varepsilon''(f)$ can be further expanded as,

$$\varepsilon'(f) = \varepsilon_\infty + \left[\frac{(\varepsilon_S - \varepsilon_\infty)\left\{1 + (\omega\tau)^\beta \cos\left(\frac{\beta\pi}{2}\right)\right\}}{1 + 2(\omega\tau)^\beta \cos\left(\frac{\beta\pi}{2}\right) + (\omega\tau)^{2\beta}} \right] + \frac{\sigma_{sp}}{\varepsilon_0 \omega^p} \tag{9}$$

and

$$\varepsilon''(f) = \left[\frac{(\varepsilon_S - \varepsilon_\infty)\left\{1 + (\omega\tau)^\beta \sin\left(\frac{\beta\pi}{2}\right)\right\}}{1 + 2(\omega\tau)^\beta \cos\left(\frac{\beta\pi}{2}\right) + (\omega\tau)^{2\beta}} \right] + \frac{\sigma_{fc}}{\varepsilon_0 \omega^p}, \tag{10}$$

where σ_{fc} and σ_{sp} are the free charge carrier and space charge carrier conductivity respectively. In Fig. 5a, b, using modified Cole–Cole model, the green lines are fitted with the experimental curves. The calculated values of the parameters are summerised in Table 2. β values are closer to unity indicating limited distribution of dielectric relaxation time. Both σ_{fc} and σ_{sp} increase with increasing temperature. Dielectric relaxation time (τ) gets smaller with the rise in temperature. This happens due to the increase in mobility of the ions with increasing temperature.

Dielectric response and dielectric relaxation process in dielectric materials can be further explained by complex electric modulus [34]. Electric modulus is defined as,

$$M^* = \frac{1}{\varepsilon^*} = \frac{\varepsilon'}{(\varepsilon')^2 + (\varepsilon'')^2} + \frac{\varepsilon''}{(\varepsilon')^2 + (\varepsilon'')^2} = M' + iM'', \tag{11}$$

Figure 5c, d exhibit the frequency variation of M' and M'' of the sample respectively. M' is almost zero in lower frequencies due to minor electrode polarisation effect. With the increase in frequency, M' increases with a transition but shows no characteristic peak. This is an intrinsic behaviour of highly capacitive system [35]. Loss peaks are observed in the curves of M'' spectra. This characteristic peak depicts the presence of ionic conduction relaxation. In the lower frequency region of the peak, immobilised charge carriers pass easily without any obstruction but in the higher frequency side of the peak, the charge carriers are restricted to the potential well [35]. Interfacial polarisation arises due to the dielectric difference between the surface shell and the core material [36]. With temperature rise, free charge accumulates at the interface in the sample. as a result relaxation time decreases. The measured data of M'' spectra can be fitted using a general solution of Modified Kohlrausch–Williams–Watts (KWW) decay function as follows,

$$M''(f) = \frac{M''_{max}}{\frac{(1 - |a - b|)}{a + b}\left[b\left(\frac{f}{f_{max}}\right)^{-a} + a\left(\frac{f}{f_{max}}\right)^b\right] + |a - b|}, \tag{12}$$

where the values of shape parameters 'a' and 'b' typically lie in between 0 and 1 (summerised in Table 3). Non-Debye type dielectric relaxation is present in the sample. The values of shape parameters become higher with temperature.

Electrode-dielectric material (the sample) junction i.e. metal–semiconductor junction forms Schottky Barrier Diode (SBD). Capacitance–bias voltage (C–V) characteristics study is a significant tool to get the idea about different Schottky parameters of SBD such as built in voltage (V_{bi}), Fermi energy (E_F), donor concentration (N_D), image force lowering $(\Delta\varphi_b)$, barrier height (φ_{C-V}) and depletion width (W_D). Well known Mott-Schottky analysis can be implied in the bias dependent depletion region of SBD. By this abovementioned analysis, the depletion capacitance is stated as follows [37–39],

$$\frac{1}{C^2} = \frac{2(V_{bi} - V)}{q\varepsilon_S \varepsilon_0 A^2 N_D}, \tag{13}$$

where A is the effective area, ε_S and ε_0 are the dielectric constants of the material and of the free space

Table 2 The derived electrical parameters [relaxation time (τ), parameter (β), exponent (p), space charge conductivity (τ), free charge conductivity (τ)] of the TMO sample from dielectric spectra analysis

Parameters	TMO sample			
	393 K	443 K	473 K	493 K
τ (s)	9.0×10^{-2}	6.0×10^{-2}	5.0×10^{-2}	4.5×10^{-3}
β	0.92	0.93	0.96	0.98
p	0.19	0.65	0.82	0.90
σ_{sc} (mho m^{-1})	5.07×10^{-9}	2.03×10^{-8}	4.97×10^{-7}	5.13×10^{-6}
σ_{fc} (mho m^{-1})	3.58×10^{-7}	5.17×10^{-6}	8.23×10^{-5}	4.77×10^{-5}

Table 3 The derived electrical parameters [shape parameters (a) and (b)] of TMO sample from electrical modulus spectra analysis

Parameters	Sample		
	443 K	473 K	493 K
a	0.64	0.98	0.99
b	0.51	0.79	0.89
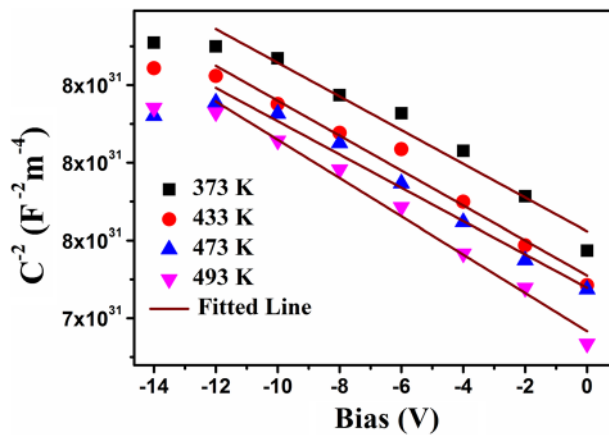
Fig. 6 $1/C^2$ versus V plot with a Mott–Schottky fit to the depletion capacitance

Table 4 The derived Schottky parameters [built in voltage (V_{bi}), Fermi energy (E_F), donor concentration (N_D), image force lowering $(\Delta\phi_b)$, barrier height (ϕ_{C-V}) and depletion width (W_D)] of Au/TMO Schottky Barrier Diode from C–V measurements

Parameters	Sample			
	393 K	443 K	473 K	493 K
V_{bi} (eV)	0.31	0.29	0.27	0.25
E_F (eV)	0.23	0.26	0.29	0.32
$N_C \times 10^{19}$ (m^{-3})	3.4	4.2	4.8	5.1
$N_D \times 10^{17}$ (m^{-3})	2.9	3.1	3.4	3.7
$W_D \times 10^{-5}$ (m)	3.79	3.77	3.73	3.78
$\Delta\phi_b \times 10^{-4}$ (eV)	1.19	1.28	1.22	1.13
ϕ_{C-V} (eV)	0.54	0.55	0.56	0.57

respectively. Plot of C^{-2} versus V characteristics at different temperatures is exhibited in Fig. 6. Linear fitting of the plot determines the values of V_{bi} and N_D which are listed in Table 4. From these values, further, the Fermi energy (E_F), effective carrier density (N_C), image force lowering $(\Delta\varphi_b)$, barrier height (φ_{C-V}) and depletion width (W_D) can be evaluated using the following equations.

$$N_C = 2\left(\frac{2\pi m_e^* k_B T}{m_0 h^2}\right)^{3/2} \tag{14}$$

where the effective mass of an electron $m_e^* = 0.98 m_0$ and m_0 is the rest mass of electron.

$$E_F = \frac{k_B T}{q}\ln\left(\frac{N_C}{N_D}\right), \tag{15}$$

$$\Delta\phi_b = \left(\frac{q^3 V_{bi} N_D}{8\pi^2 \varepsilon_S^3}\right)^{1/4}, \tag{16}$$

$$\phi_{C-V} = V_{bi} + E_F + \Delta\phi_b, \tag{17}$$

and

$$W_D = \sqrt{\frac{2\varepsilon_S V_{bi}}{q N_D}}. \tag{18}$$

The calculated Schottky parameters values are summerised in Table 4. Barrier height (ϕ_{C-V}) slightly increases with temperature. W_D decreases with increase in temperature as excess capacitance exists at metal–semiconductor junction interface. This unique property makes the material suitable for photocatalytic and solar cell applications.
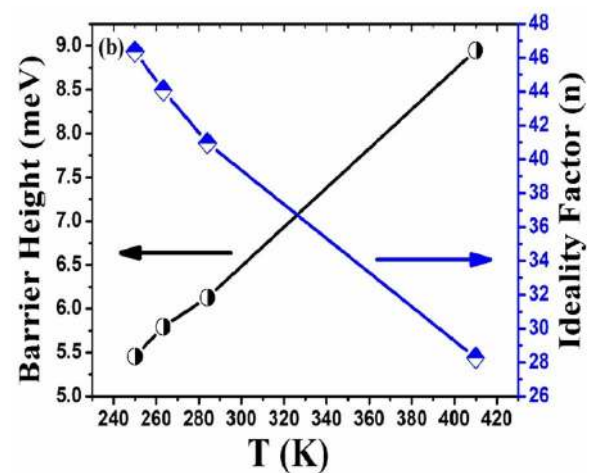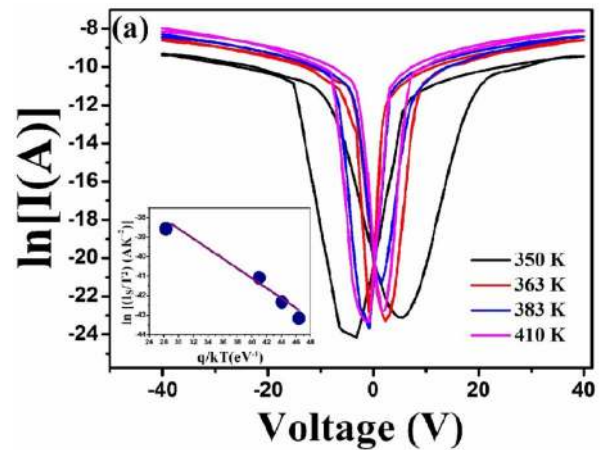
Fig. 7 **a** ln I versus V curves at different experimental temperatures (the inset displays the Richardson plot of ln (I_S/T^2) versus q/kT of the sample), **b** variation of barrier height and variation of ideality factor with temperature

The thermionic current–voltage (I–V) characteristics of the Au/TMO/Au Schottky diode have been measured within the voltage range ±40 V. Figure 7a shows ln I versus V plots at different temperatures. The sample exhibits hysteresis loop in I–V characteristics curve. Here the least value of current shifts from zero voltage. Generally, the ferroelectric property of the material shifts the curves from their original position because of polarisation hysteresis. But in this case, TMO exhibits ferroelectricity only below its Neel temperature (~41 K). The electrical hysteresis in I–V curve probably comes from the irreversible charge transport in the schottky barriers. Kim et al. [40] observed the similar ferroelectric-like hysteresis loop originated from non ferroelectric effects. Even in the absence of polarisation switching effect; several factors such as electrostatic interaction, electrochemical strain etc. are responsible for the charge injection between forward and reverse bias sweep. Due to this unique property, the sample may pose electrical memory effect. Using thermionic emission (TE) theory, rectifying nature of I–V characteristics of a SBD is stated by Richardson formalism [41],

$$I = I_S \left[\exp \left\{ q(V - IR)/nk_B T \right\} - 1 \right], \quad (19)$$

where I is the forward current. Reverse saturation current (I_S) is written as

$$I_S = AA * T^2 \exp \left(-\frac{q\phi_b}{k_B T} \right), \quad (20)$$

where A is the area of the sample, A^* is a constant, n is the ideality factor, ϕ_b is the barrier height and k_B is Boltzmann's constant. Reverse saturation current increases with rise in temperature. Figure 7b shows the temperature variation of ideality factor and barrier height. With temperature, ϕ_b increases but n decreases. For ideal Schottky diode n=1, but in practical case n is always greater than 1. The barrier inhomogeneity of SBD interface causes the high value of n [42]. Richardson plot of ln $\left(I_S/T^2 \right)$ versus $q/k_B T$ is shown in the inset of Fig. 7a. The plot is linear in nature because of the inhomogeneous nature of the sample [43]. The obtained value of ϕ_b from I–V study is greater than that from C–V analysis. The presence of excess capacitance and heterogenous barrier at Au–TMO interface are the responsible factors [37]. From the temperature dependent current–voltage characteristics in forward bias, the parameters such as series resistance (R_S), ideality factor (n) can be evaluated using the model of Cheung and Cheung [44]. According this model, current–voltage characteristics of a SBD can be expressed as,
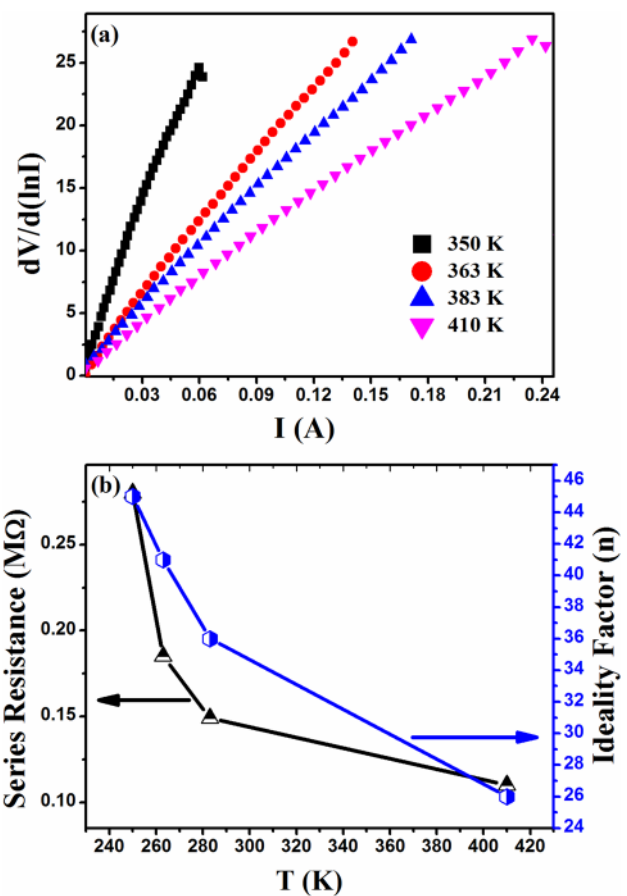
$$\frac{dV}{d \ln I} = IR_S + \frac{nk_B T}{q}, \quad (21)$$

Fig. 8 **a** Temperature dependent plot of $dV/d \ln I$ versus I at different experimental temperatures, **b** variation of series resistance and ideality factor with temperature

Figure 8a shows the linear variation of $dV/d \ln I$ versus I plots at various measuring temperatures. The parameters i.e. R_S and n are evaluated from the linear plots in Fig. 8a. The temperature variation of R_S and n is shown in Fig. 8b. The values of ideality factor from Cheung's approach are almost similar to those evaluated from Richardson's equation in TE theory. This result implies the validity and the consistency of these models. From the results, it can be depicted that the defect states present in the TMO interface layer are the dominant responsible factor for the charge transport phenomenon. The series resistance value increases with the decrease in temperature. Here, defect state density decreases with lowering temperature [37].

To measure magnetic susceptibility of the material, Evans balance method is used here. Mass magnetic susceptibility, χ_g, is written as [45],

$$\chi_g = \left[C_{bal} L (R - R_0) \right] / \left(m \times 10^9 \right), \quad (22)$$

where C_{bal} is a constant, L is sample height, m is sample mass. R and R_0 are the digital readings for sample filled tube

and empty tube respectively. Room temperature effective magnetic moment $\left(\mu_{eff}\right)$ is calculated using the following equation,

$$\mu_{eff} = 2.828 \times \sqrt{M\chi_g T}\,\mu_B, \tag{23}$$

where M is the molar mass of TMO, μ_B is Bohr magneton. μ_{eff} of the sample is ~0.11 μ_B showing paramagnetic behaviour of TMO at room temperature. The paramagnetic nature of the sample may discard the possibility of multiferroicity of the sample at room temperature. Wang et al., Rai et al. and Ponomarev et al. [46–48] reported the presence of magnetoelectric coupling in the paramamagnetic state of metal–organic framework and rare earth molybdates respectively. In the present sample, further study is done to observe the nature of magnetoelectric coupling at room temperature. An applied magnetic field affects the magnetic order as well as the dielectric constant of a magnetoelectric material [49]. Figure 9a and the inset of Fig. 9a shows frequency dependence of dielectric constant $\left(\varepsilon^{/}\right)$ and dielectric loss (tan δ) with and without magnetic field respectively. With the application of magnetic field, there exists a slight change in dielectric constant. With the application of magnetic field, dielectric loss (leakage current) slightly decreases throughout the probing frequency range. The change in the value of $\varepsilon^{/}$ and tan δ is higher in low frequency region than that of high frequency range. It suggests that the grain boundaries are more sensitive to the magnetic field than the intrinsic grains [48]. Figure 9b shows the magnetic field dependence of dielectric loss (tan δ) at different frequencies. The loss reduces with the increase in applied magnetic field. The room temperature magnetocapacitance/magnetodielectric (MD) response as a function of applied magnetic field H measured at different frequencies is shown in Fig. 9c. Magnetodielectric response can be expressed using the following equation,

$$MD = \frac{\varepsilon^{/}(H) - \varepsilon^{/}(0)}{\varepsilon^{/}(0)} \times 100, \tag{24}$$

where $\varepsilon^{/}(H)$ and $\varepsilon^{/}(0)$ represent the value of dielectric constant corresponding to the magnetic field H and zero respectively. The increasing magnetic field gives rise to the enhanced negative magnetocapacitance at room temperature. To explain the magnetic field dependency of dielectric constant, a recently proposed model of a two-phase inhomogeneous system can be introduced [50]. According to this model, a composite medium having different conductivities possesses Maxwell–Wagner polarisation between the interface which in turn causes magnetodielectric effect without multiferroicity. In the present case, considering TMO sample as a inhomogeneous medium, the magnetodielectric effect arises not
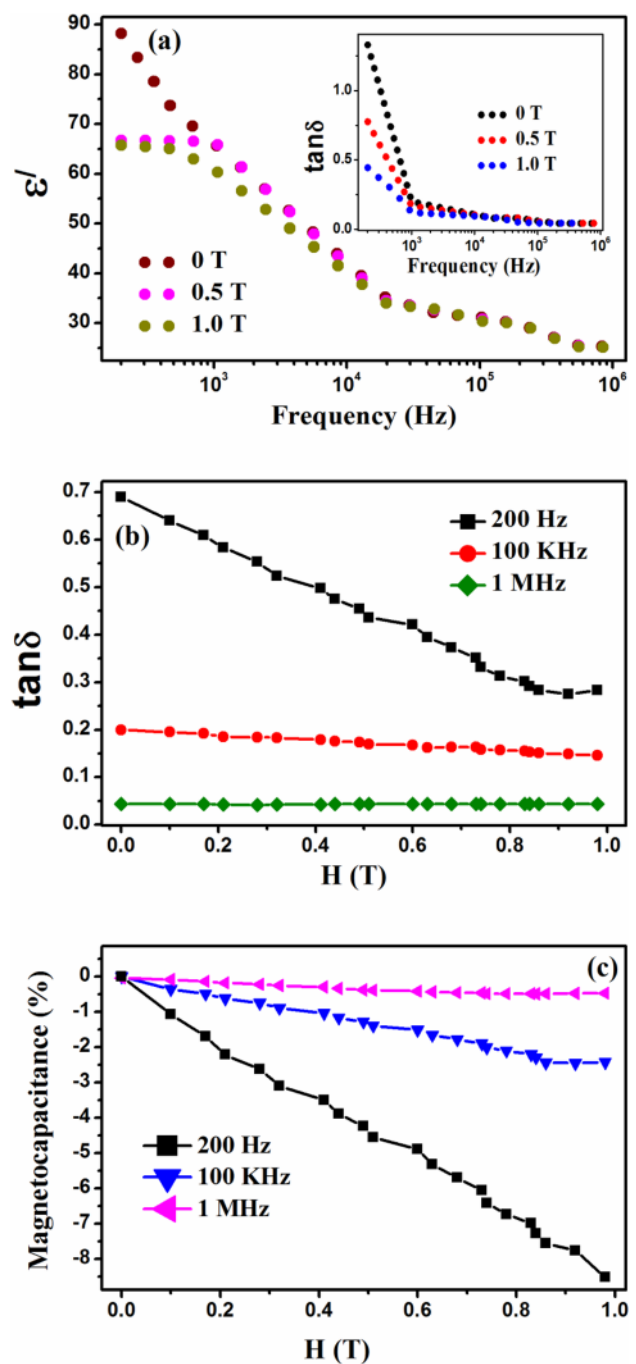
Fig. 9 a The frequency variation of dielectric constant $\left(\varepsilon^{/}\right)$ at different applied magnetic fields (the inset display the frequency variation of dielectric loss (tan δ) at different applied magnetic fields), **b** magnetic field dependence of dielectric loss (tan δ) at different frequencies, **c** magnetic field dependence of magnetodielectric (MD) effect at different frequencies

because of multiferroicity, but due to the Maxwell–Wagner space charge at the interface and the effect of magnetic field thereon. When magnetic field is applied, it generates an electric field which influences the polarisation of

the system by reducing the accumulated charge in the interface. As a result, the value of dielectric constant also decreases [51].

4 Conclusion

To summarise, we have investigated dielectric and magnetodielectric properties of mesoporous Terbium Manganate (TMO) nanoparticles (NPs). The sample exhibits relatively high surface area (20.9 m^2 g^{-1}) and narrow pore size distribution. Dielectric response of the material to the external alternating field is described by modified Cole–Cole model. Modified Electric modulus spectra is well explained by KWW function. The capacitive system of electrode-TMO junction forms Schottky Barrier Diode (SBD) which is well explained by thermionic emission theory from the I–V measurements. Ferroelectric-type hysteretic behaviour is observed in the sample. Different barrier properties are well explained by Mott–schottky analysis in the depletion region. Although TMO exhibits paramagnetic nature at room temperature, it responds to the applied transverse magnetic field by showing significant change in dielectric constant over a broad frequency window. The negative magnetodielectric effect may be attributed to the presence of inhomogeneity in the sample. These observations demonstrate that the perovskite TMO is a promising multifunctional material, showing dielectric, magnetodielectric properties at room temperature.

Compliance with ethical standards

Conflict of interest The author(s) declare that they have no competing interests.

References

1. Kumar RD, Thangappan R, Jayavel R (2017) Study on the effect of annealing temperature and photocatalytic properties of TbMnO$_3$ nanoparticles. Optik 138:365–371
2. Lahmar A, Habouti S, Dietze M, Solterbeck CH, Es-Souni M (2009) Effects of rare earth manganites on structural, ferroelectric, and magnetic BiFeO$_3$ properties of thin films. Appl Phys Lett 94:012903(1–3)
3. Lin GJ, Yang H, Xian T, Wei ZQ, Jiang JL, Feng WJ (2012) Synthesis of TbMnO$_3$ nanoparticles via a polyacrylamide gel route. Adv Powder Technol 23:35–39
4. Lone IH, Aslam J, Radwan NRE, Bashal AH, Ajlouni AFA, Akhter A (2019) Multiferroic ABO$_3$ transition metal oxides: a rare interaction of ferroelectricity and magnetism. Nanoscale Res Lett 14(1):1–12
5. Lu C, Cui Y (2012) Dielectric characteristics of cation deficient TbMnO$_3$. Phys B 407(18):3856–3860
6. Liu ZK, Qi YJ, Lu CJ (2010) High efficient ultraviolet photocatalytic activity of BiFeO$_3$ nanoparticles synthesized by a chemical coprecipitation process. J Mater Sci Mater Electron 21:380–384
7. Yin WJ, Weng B, Ge J, Sun Q, Li Z, Yan Y (2019) Oxide perovskites, double perovskites and derivatives for electrocatalysis, photocatalysis, and photovoltaics. Energ Environ Sci 12:442–462
8. Shin SS, Lee SJ, Seok SI (2019) Exploring wide bandgap metal oxides for perovskite solar cells. APL Mater 7:022401(1–9)
9. Belessi VC, Trikalitis PN, Ladavos AK, Bakas AK, Pomonis PJ (1999) Structure and catalytic activity of La$_{1-x}$FeO$_3$ system (x = 0.00, 0.05, 0.10, 0.15, 0.20, 0.25, 0.35) for the NO + CO reaction. Appl Catal A 177(1):53–68
10. Cuartero V, Blasco J, Rodríguez-Velamazán JA, García J, Subías G, Ritter C (2013) Transitions induced by a magnetic field in slightly doped TbMnO$_3$. Solid State Sci 21:37–43
11. Zabihi F, Tebyetekerwa M, Xu Z, Ali A, Kumi AK, Zhang H, Jose R, Ramakrishna S, Yang S (2019) Perovskite solar cell-hybrid devices: thermoelectrically, electrochemically, and piezoelectrically connected power packs. J Mater Chem A 7(47):26661–26692
12. Acharya SA, Khule SM, Gaikwad VM (2015) Investigation of multiferroic behaviour of TbMnO$_3$ nanoplates. Mater Res Bull 67:111–117
13. Kimura T, Goto T, Shintani H, Ishizaka K, Arima T, Tokura Y (2003) Magnetic control of ferroelectric polarization. Nature 426:55–58
14. Gupta PK, Ghosh S, Kumari S, Pal A, Roy S, Singh R, Singh P, Singh RK, Ghosh AK, Chatterjee S (2019) Spin phonon coupling and magneto-dielectric coupling in BiFeO$_3$—TbMnO$_3$ composite. Mater Res Express 6(8):086114
15. Lu C, Cui Y (2014) Dielectric characteristics of Si-added and Si-doped TbMnO$_3$. Phys B 432:58–63
16. Izquierdo JL, Astudillo A, Bolaños G, Zapata VH, Morán O (2015) Dielectric response of Al-substituted multiferroic TbMnO$_3$ at high temperatures. Ceram Int 41(1):1285–1296
17. Halder M, Das AK, Meikap AK (2019) Study of optical and thermal properties of terbium manganate nanoparticles. Indian J Phys 93(12):1591–1600
18. Zheng M, Zhang H, Gong X, Xu R, Xiao Y, Dong H, Liu X, Liu Y (2013) A simple additive-free approach for the synthesis of uniform manganese monoxide nanorods with large specific surface area. Nanoscale Res Lett 8:166(1–7)
19. Yang S, Yang H, Ma H, Guo S, Cao F, Gong J, Deng Y (2011) Manganese oxide nanocomposite fabricated by a simple solid-state reaction and its ultraviolet photoresponse property. Chem Commun 9:2619–2621
20. Innocent B, Pasquier D, Ropital F, Hahn F, Léger JM, Kokoh KB (2010) FTIR spectroscopy study of the reduction of carbon dioxide on lead electrode in aqueous medium. Appl Catal B 94(3–4):219–224
21. Storck S, Bretinger H, Maier WF (1998) Review of gas adsorption. Appl Catal A-Gen 174:137–140
22. Gregg SJ, Sing KSW (1982) Adsorption, surface area and porosity, 2nd edn. Academic Press, London
23. Yu JC, Xu A, Zhang L, Song R, Wu L (2004) Synthesis and characterization of porous magnesium hydroxide and oxide nanoplates. J Phys Chem B 108:64–70
24. Zhang PF, Wang L, Yang SZ, Schott JA, Liu XF, Mahurin SM, Huang CL, Zhang Y, Fulvio PF, Chisholm MF, Dai S (2017) Solid-state synthesis of ordered mesoporous carbon catalysts via a mechanochemical assembly through coordination cross-linking. Nat Commun 8:15020(1–10)

25. Zhou M, Wei Z, Qiao H, Zhu L, Yang H, Xia T (2009) Particle size and pore structure characterization of silver nanoparticles prepared by confined arc plasma. J Nanomater 2009:968058(1–5)

26. Fagerlund G (1973) Determination of specific surface by the BET method. Mater Struct 6:239–245

27. Tan YH, Davis JA, Fujikawa K, Ganesh NV, Demchenko AV, Stine KJ (2012) Surface area and pore size characteristics of nanoporous gold subjected to thermal, mechanical, or surface modification studied using gas adsorption isotherms, cyclic voltammetry, thermogravimetric analysis, and scanning electron microscopy. J Mater Chem 14:6733–6745

28. Lowell S, Shields JE, Thomas MA (2004) Characterization of porous solids and powders: surface area, pore size, and density. Kluwer Academic Publishers, Dordrecht

29. Khajonrit J, Prasoetsopha N, Sinprachim T, Kidkhunthod P, Pinitsoontorn S, Maensiri S (2017) Structure, characterization, and magnetic/electrochemical properties of Ni-doped $BiFeO_3$ nanoparticles. Adv Nat Sci-Nanosci 8:015010(1–12)

30. Soleymani M, Moheb A, Joudaki E (2009) High surface area nano-sized $La_{0.6}Ca_{0.4}MnO_3$ perovskite powder prepared by low temperature pyrolysis of a modified citrate gel. Cent Eur J Chem 7(4):809–817

31. Rabelo AA, Macedo MC, Melo DMA, Paskocimas CA, Martinelli AE, Nascimento RM (2011) Synthesis and characterization of $La_{1-x}Sr_xMnO_{3\pm\delta}$ powders obtained by the polymeric precursor route. Mater Res 14:91–96

32. Dong M, Reau JM, Ravez J, Gitae J, Hagenmuler PJ (1995) Impedance spectroscopy analysis of a $LiTaO_3$-type single crystal. J Solid State Chem 116:185–192

33. Abdelkafi Z, Abdelmoula N, Khemakhem H, Bidault O, Maglione M (2006) Dielectric relaxation in $BaTi_{0.85}(Fe_{1/2}Nb_{1/2})_{0.15}O_3$ perovskite ceramic. J Appl Phys 100:114111(1–7)

34. Yeriskin SA, Balbasi M, Tataroglu A (2016) Frequency and voltage dependence of dielectric properties, complex electric modulus, and electrical conductivity in Au/7% graphene doped-PVA/n-Si (MPS) structures. J Appl Polym Sci 133(23):43827

35. Halder M, Meikap AK (2019) Influence on loading terbium manganate on optical, thermal and electrical properties of polyvinyl alcohol nanocomposite films. J Mater Sci Mater Electron 30(5):4792–4806

36. Sinha R, Kundu S, Basu S, Meikap AK (2016) Effect of La doping on optical and electrical transport properties of nanocrystalline $YCrO_3$. Solid State Sci 60:75–84

37. Mahato S, Biswas D, Gerling LG, Voz C, Puigdollers J (2017) Analysis of temperature dependent current–voltage and capacitance–voltage characteristic of an Au/V2O5/n-Si Schottky diode. AIP Adv 7:085313(1–11)

38. Kalon G, Shin YJ, Truong VG, Kalitsov A, Yang H (2011) The role of charge traps in inducing hysteresis: capacitance–voltage measurements on top gated bilayer graphene. Appl Phys Lett 99:083109(1–4)

39. Almora O, Aranda C, Marzá EM, Belmonte GG (2016) On Mott–Schottky analysis interpretation of capacitance measurements in organometal perovskite solar cells. Appl Phys Lett 109:173903(1–6)

40. Kim B, Seol D, Lee S, Lee HN, Kim Y (2016) Ferroelectric-like hysteresis loop originated from non-ferroelectric effects. Appl Phys Lett 109:102901(1–6)

41. Yeganeh MA, Rahmatollahpur SH (2010) Barrier height and ideality factor dependency on identically produced small Au/p-Si Schottky barrier diodes. J Semicond 31(7):074001(1–6)

42. Halder M, Das AK, Meikap AK (2018) Effect of $BiFeO_3$ nanoparticle on electrical, thermal and magnetic properties of polyvinyl alcohol (PVA) composite film. Mater Res Bull 104:179–187

43. Sharma M, Tripathi SK (2012) Temperature dependent current-voltage (IV) characteristics of Al/n-Cadmium Selenide-Polyvinyl alcohol (Al/n-CdSe-PVA) Schottky diode. Optoelectron Adv Mat 6(1–2):200–204

44. Cheung SK, Cheung NW (1986) Extraction of Schottky diode parameters from forward current–voltage characteristics. Appl Phys Lett 49(2):85–87

45. Evans DF (1974) A new type of magnetic balance. J Phys E: Sci Instrum 7(4):247–248

46. Wang W, Yan LQ, Cong JZ, Zhao YL, Wang F, Shen SP, Zou T, Zhang D, Wang SG, Han XF, Sun Y (2013) Magnetoelectric coupling in the paramagnetic state of a metal–organic framework. Sci Rep 3:2024(1–5)

47. Ponomarev BK, Evanov SA, Red'kin BS, Kurlov VN (1992) Magnetoelectrical effect in paramagnetic rare-earth molybdates. Phys B 177(1–4):327–329

48. Rai HM, Late R, Saxena SK, Mishra V, Kumar R, Sagdeo PR, Sagdeo A (2015) Room temperature magnetodielectric studies on Mn-doped $LaGaO_3$. Mater Res Express 2:096105(1–9)

49. Adhlakha N, Yadav KL (2014) Study of dielectric, magnetic and magnetoelectric behavior of (x) NZF-(1−x) PLSZT multiferroic composites. IEEE Trans Dielectr Electr Insul 21(5):2055–2061

50. Lawes G, Tackett R, Adhikary B, Naik R, Masala O (2006) Positive and negative magnetocapacitance in magnetic nanoparticle systems. Appl Phys Lett 88:242903(1–4)

51. Banerjee S, Hajra P, Datta A, Bhaumik A, Mada M, Bandyopadhyay S, Chakravorty D (2014) Magnetodielectric effect in $Ni_{0.5}Zn_{0.5}Fe_2O_4$–$BaTiO_3$ nanocomposites. Bull Mater Sci 37(3):497–504